Journal of Materials Science & Technology 220 (2025) 199–209

Contents lists available at ScienceDirect

Journal of Materials Science & Technology

journal homepage: www.elsevier.com/locate/jmst

Research Article

Fast diffusion and stable topotactic reaction in single crystal conversion anode

Weili Liu[a,1], Tian Xu[a,1], Shouguo Wang[b], Guanglin Xia[a], Dalin Sun[a], Xuebin Yu[a,*]

[a] Department of Materials Science, Fudan University, Shanghai 200433, China
[b] Anhui Key Laboratory of Magnetic Functional Materials and Devices, School of Materials Science and Engineering, Anhui University, Hefei 230601, China

ARTICLE INFO

Article history:
Received 3 February 2024
Revised 1 September 2024
Accepted 1 September 2024
Available online 27 September 2024

Keywords:
Conversion electrodes
Single-crystal
SnO_2
Topotactic reaction
Na-ion batteries

ABSTRACT

Conversion electrodes typically have high theoretical specific capacity, but mostly suffer large structural changes during charge/discharge and result in poor cycling stability. The optimization of the polycrystalline materials is the mostly used strategy, however, these polycrystalline materials are intrinsically vulnerable to grain-boundary (intergranular) fracture caused by the anisotropic volume change during sodiation/desodiation, resulting in rapid impedance growth and capacity decay. Herein, we propose an alternative pathway to design single-crystal materials as potential conversion anodes. As an example, SnO_2 with different crystallinities is successfully synthesized via solvothermal methods and compared to determine the implications of different crystallinity for the electrochemical properties of conversion anodes. It is demonstrated that the single-crystal SnO_2 not only has faster Na^+ diffusion dynamics but also maintains structural stability via topotactic reaction. Further optimization of the electron conduction and structural robustness is realized by uniformly covering a graphitic carbon shell on the surface of single-crystal SnO_2 nanosheets. The modified single-crystal SnO_2 exhibits a high reversible capacity of 436.2 mA h g^{-1} and maintains a high capacity of 257.1 mA h g^{-1} and remarkable capacity retention of about 98.9 % after 9000 cycles at 5000 mA g^{-1}. The deep understandings of the topotactic reaction in single crystal conversion anode in this work provide a theoretical foundation and new direction for further developing electrode materials with excellent electrochemical performance, especially high rate capabilities, and long cyclability.

1. Introduction

Conversion-based compounds M_aX_b (M = Fe, Co, Ni, Cu, Sn, Ge; X = O, S, F, P, N), particularly oxides (e.g., SnO_2, CoO, NiO), have received great interest due to their much higher capacity than the intercalation-based electrodes for use in sodium-in batteries (NIBs) [1-6]. In contrast to the topotactic transformation mechanism of the intercalation type electrodes [7], the conversion type electrodes have a more complex reaction mechanism, involving sodium ion transport and M or A ions migration/rearrangement [6,8-10]. In polycrystalline materials, the M or A ions migration/rearrangement causes the spatial distribution and decoupling of the converted products from the host, resulting in nonuniform phases [11,12]. Moreover, sodium ion transport in polycrystals leads to large volume expansion, which causes the pulverization of the electrodes and the irreversible reaction [6]. Both of these factors are the reason for the poor cycling of conversion electrodes, which is the major obstacle to their commercialization [11-16].

With the aim of enhancing their performance, much effort has been focused on nanostructuring materials to promote the efficient reaction with Na [17-20]. In this respect, metal oxides, particularly SnO_2, have been studied frequently as conversion compounds due to their low cost and straightforward synthesis [21]. It has been demonstrated that synthesizing metal oxides with nanostructures, such as hollow or porous structures, one-dimensional nanorods/nanowires/nanotubes, and two-dimensional nanosheets, is effective in sustaining the volume variation [17-21]. These engineered oxides have shown enhanced rate capability and cyclability, however, long-term stability still remains a challenge for nanostructured conversion compounds [22].

As an alternative to nanostructures, recent studies have shown that the formation of amorphous structures is an efficient route to improve the electrochemical performance of electrode materials [23-27]. For example, amorphous Fe_2O_3 nanoshells deposited on carbonized bacterial cellulose nanofibers (A-Fe_2O_3@CBC) delivered

* Corresponding author.
E-mail address: yuxuebin@fudan.edu.cn (X. Yu).
[1] These authors contributed equally to this work.

https://doi.org/10.1016/j.jmst.2024.09.013
1005-0302/

a high specific capacity of 1135 mA h g^{-1} over 200 cycles, remarkably exceeding the capacities of crystalline counterpart [28]. The intrinsically isotropic amorphous structure not only provides rich ion diffusion pathways but also buffer volume expansion resulting from sodium insertion [25]. However, amorphous materials need hybridization with a large amount of conductive materials to suppress their agglomeration resulting from their intrinsic instability and enhance their electrical conductivity, which ultimately leads to low energy density [29].

Recently, it has been demonstrated that a single crystal can eliminate the internal grain boundaries and inter-granular fracture, thus improving the intrinsic ion intercalation and cycling stability of the intercalation compounds [30–36]. For instance, Dahn's group [32,33] has confirmed that single-crystal cathode materials have superior long-term charge-discharge cycle lifetime compared to conventional polycrystalline. Li's group [36] has reported that single-crystal H-type Nb_2O_5 has fast Li-(de)intercalation kinetics and excellent cycling stability by homogenizing the conductivity of the surrounding electrons and lithium ions. These results suggest that a single crystal may also possess outstanding intrinsic fast kinetics, high specific capacity, and excellent cycling stability for the conversion electrodes.

This work employs SnO_2 as a model material to determine the implications of different crystallinity for the electrochemical properties. Single crystalline (s-SnO_2) nanosheets, polycrystalline (p-SnO_2) nanosheets, and amorphous clusters (a-SnO_2) of SnO_2 are synthesized via a solvothermal method. Among the three crystallinities, s-SnO_2 shows the best performance in enhancing the electrical/ion conductivity and maintaining structural stability via topotactic reaction. Further optimization of the electron conduction and structural robustness was realized by uniformly covering a graphitic carbon shell on the surface of s-SnO_2 nanosheets. The deep understandings of the topotactic reaction in single crystal conversion anode in this work provide a theoretical foundation and new direction for further developing electrode materials with excellent electrochemical performance, especially high rate capabilities, and long cyclability.

2. Results

Fig. 1 shows the schematic illustration for the formation of SnO_2 with different crystallinity. During the synthesis of s-SnO_2 and p-SnO_2 nanosheets (as shown in Fig. 1(a, b)), the tin cation ions electrostatically interacted with ethanolamine anionic ions, resulting in the formation of Sn-ethanolamine complexes. The ethanolamine anionic ions tended to preferentially adsorb on the highly reactive facets, which was demonstrated by previous studies [37,38] when these complexes then underwent atomic assembly to form thin two-dimensional structures at a temperature of 180 °C through solvothermal reaction. Without stirring, the

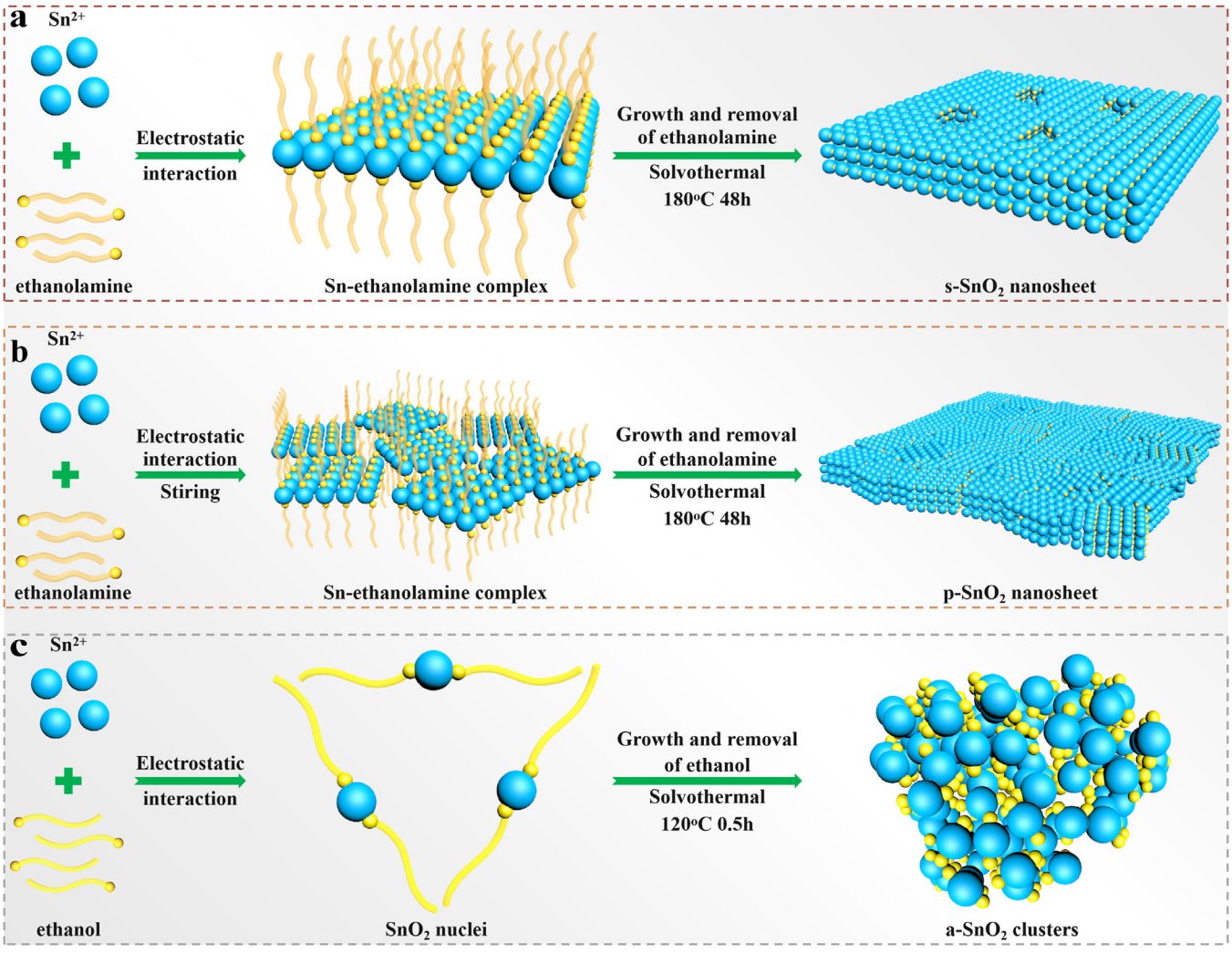

Fig. 1. Schematic illustration for the formation of (a) single crystal SnO_2 nanosheet, (b) polycrystal SnO_2 nanosheet, and (c) amorphous SnO_2 clusters.

small thin two-dimensional structures slowly grew into larger s-SnO_2 nanosheets with numerous pits on their surfaces (Fig. 1(a)), while with stirring, the small thin two-dimensional structures grew into larger p-SnO_2 nanosheets due to their disorder in directions (Fig. 1(b)). For the a-SnO_2 clusters, SnO_2 initially nucleated at 120 °C and then quickly grew into clusters (Fig. 1(c)). Afterwards, a carbon layer was uniformly applied onto the s-SnO_2 nanosheet through in situ polymerization of dopamine at room temperature. Subsequently, the resulting s-SnO_2@C nanosheets were subjected to post-calcination at 450 °C under an argon atmosphere.

The morphologies and crystallinity of s-SnO_2, p-SnO_2, and a-SnO_2 nanomaterials are confirmed by field-emission scanning electron microscope (SEM) and TEM images, as shown in Fig. 2. The resultant s-SnO_2 nanosheets are monodisperse with the size of 100–800 nm and thickness of 5–10 nm, and present smooth surfaces (Figs. 2(a, b) and S1(a–c) in Supplementary materials). The TEM images and corresponding selected area electron diffraction (SAED) pattern provide evidence that each individual nanosheet exhibits characteristics of a single crystal structure (Fig. 2(b, inset)). The SAED patterns can be matched to the diffraction spots of the [001] zone (Fig. S2) [39]. Furthermore, a high-resolution TEM image reveals the presence of atomic planes such as (110), (200), and (101) with lattice spacings measuring 0.334, 0.244, and 0.274 nm, respectively. Notably, numerous pits are observable on the surface of the nanosheet (Fig. 2(c)). According to the crystallographic symmetries of tetragonal SnO_2, the flat surfaces of s-SnO_2 exhibit facets dominated by the {110} planes. Elemental mapping indicates a homogeous distribution of Sn and O with a stoichiometric ratio as designed (Fig. S3). For comparison, p-SnO_2 is found to contain many internal pores (Figs. 2(d, e) and S4) and intergranular boundaries (GB) (Fig. 2(f, inset)) with similar morphologies as s-SnO_2 nanosheets. The inserted SAED pattern illustrates a well-resolved set of concentric rings (inset in Fig. 2(e)), which can be indexed as (110), (101), (200), (211), and (301) (Fig. S5), further confirming the polycrystallinity of p-SnO_2. For the a-SnO_2 clusters, large agglomerates are observed in the SEM images as shown in Figs. 2(g) and S6, and indistinct subnanoclusters are observed in the TEM images as shown in Fig. 2(h). The HRTEM image of a-SnO_2 indicated the presence of multiple subnanoclusters composed of SnO_2 atoms, which lacked distinct lattice fringes (Fig. 2(i)). This observation suggests that the clusters of a-SnO_2 possess an amorphous structure.

The structural characteristics of the as-prepared products were assessed using X-ray diffraction (XRD) and Raman spectroscopy (Figs. 3(a) and S7(a)). Four apparent peaks in the XRD patterns (Fig. 3(a)) were assigned to diffraction from {110}, {101}, {200}, and {211} planes of tetragonal structure SnO_2 (cassiterite, JCPDS No. 88-0287), respectively. No other phases can be detected by XRD,

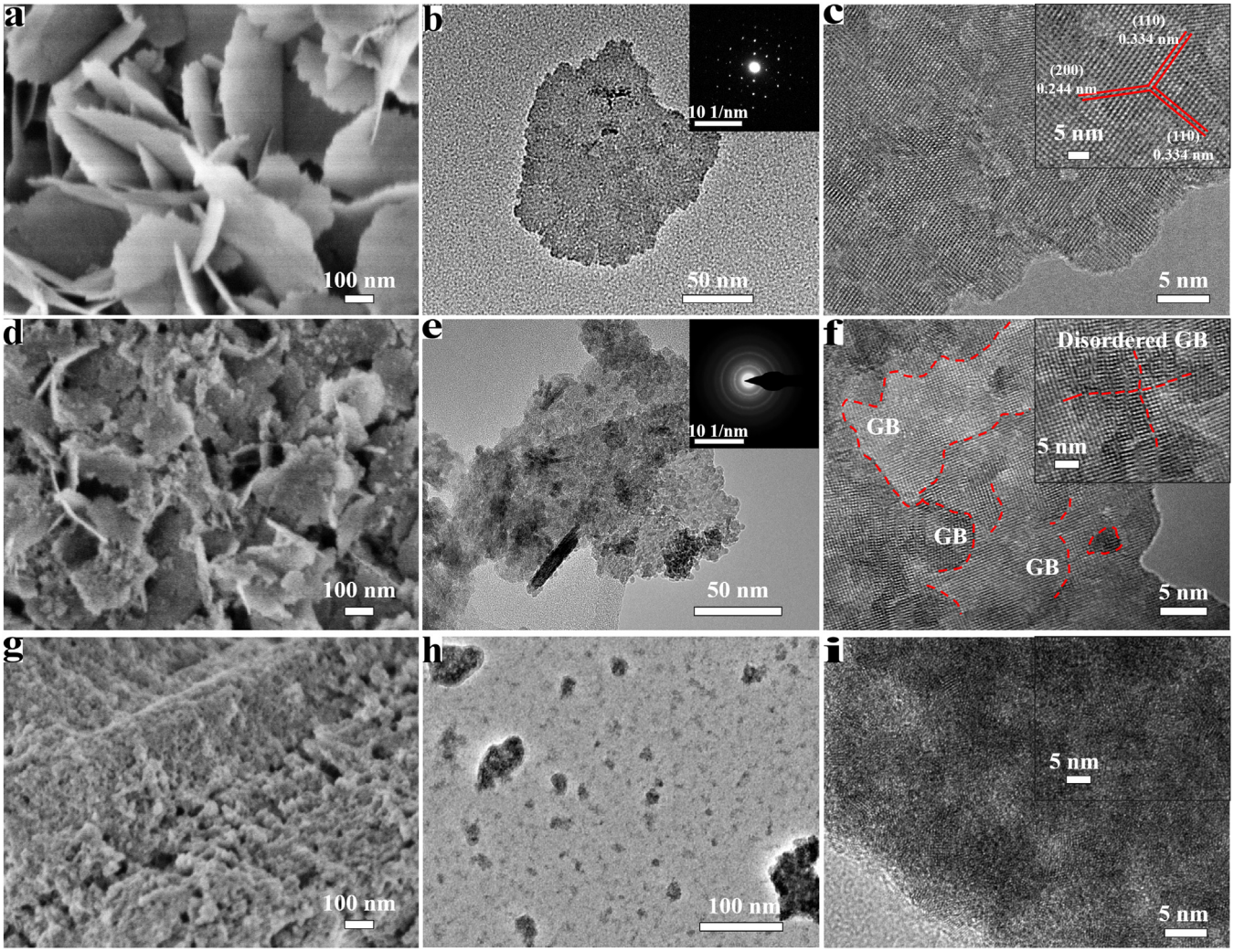

Fig. 2. (a) SEM, (b) TEM (insets: the corresponding electron-diffraction pattern) and (c) HRTEM (insets: enlarged HRTEM) images of s-SnO_2 nanosheet; (d) SEM, (e) TEM (insets: the corresponding electron-diffraction pattern), and (f) HRTEM (insets: enlarged HRTEM) images of p-SnO_2 nanosheet; (g) SEM, (h) TEM, and (i) HRTEM (insets: enlarged HRTEM) images of a-SnO_2 clusters.

suggesting that the pure SnO_2 with a tetragonal structure is obtained. For s-SnO_2, the XRD peaks of {101}, {200} diffraction shifted to the left, indicating that the interplanar spacing of {101}, {200} planes became larger, which is consistent with the results of HRTEM and SAED (inset of Figs. 2(c), S1(d), and S2). By sharp contrast, no diffraction peaks of a-SnO_2 are detected, confirming the successful formation of amorphous SnO_2. Raman spectra were further used to verify the successful preparation of only one f s-SnO_2, p-SnO_2, a-SnO_2 (Fig. S7(a)). Both the Raman spectra of s-SnO_2 and p-SnO_2 have only a single scattering peak at 587 cm^{-1}. This occurrence can be attributed to the presence of small granule size, resulting in vacant lattice sites and localized lattice disorder such as individual oxygen vacancies and their complexes within the product.

Hence, the identification of prominent Raman-scattering peaks in the spectra provides evidence for the high crystallinity of the synthesized samples. Compared to s-SnO_2 and p-SnO_2, the peak intensity of a-SnO_2 exhibits a significant reduction owing to the presence of extensive long-range correlated structural disorder. The X-ray photoelectron spectroscopy (XPS) technique was employed to investigate the chemical state of SnO_2 with different crystallinities. The presence of distinct peaks corresponding to Sn 3d 3/2 and Sn 3d 5/2 in the refined spectrum of Sn 3d provides evidence that the Sn atoms exist in the form of SnO_2 (Fig. S7(b, c)). The carbon-coated s-SnO_2 nanosheets show similar XRD patterns (Fig. 3(b)) and nanosheets morphology of single crystal structure with s-SnO_2 (Fig. 3(b, d–g)), besides the uniform and highly graphitized carbon layer around the s-SnO_2 nanosheets, which was demonstrated by the HRTEM, Raman spectrum and XPS results (Figs. 3(c, h, i) and S8).

Electrochemical measurements were carried out to compare the sodium storage properties of these SnO_2 materials with different crystallinity. Fig. 4(a) shows the first voltage profiles of a-SnO_2, p-SnO_2, and s-SnO_2 at a current density of 100 mA g^{-1}. The discharge capacity of a-SnO_2 is 2544 mA h g^{-1}, but the charge capacity is only 142 mA h g^{-1}. In simpler terms, the initial loss of capacity that cannot be reversed is approximately 2402 mA h g^{-1}, resulting in a low initial efficiency of only 5.6 % during charging. This suggests that a-SnO_2 exhibits limited electrochemical activity as anodes for NIB due to its insulating electronic properties and leads to significant decomposition of the electrolyte owing to its extensive surface area (Fig. 2(h, i)) [27]. Meanwhile, the p-SnO_2 anode delivers a slightly improved charge capacity of 162 mA h g^{-1} with an improved initial Coulomb efficiency of 19.6 %, while the charge capacity and initial Coulomb efficiency of s-SnO_2 were significantly enhanced, reaching 320 mA h g^{-1} and 42.5 %, respectively. After conformally coating carbon layers, the homogeneity of electron and ion conductivity surrounding the s-SnO_2 nanosheets was optimized, giving the s-SnO_2@C with high charge capacity and initial Coulomb efficiency of 436.2 mA h g^{-1} and 50 %,

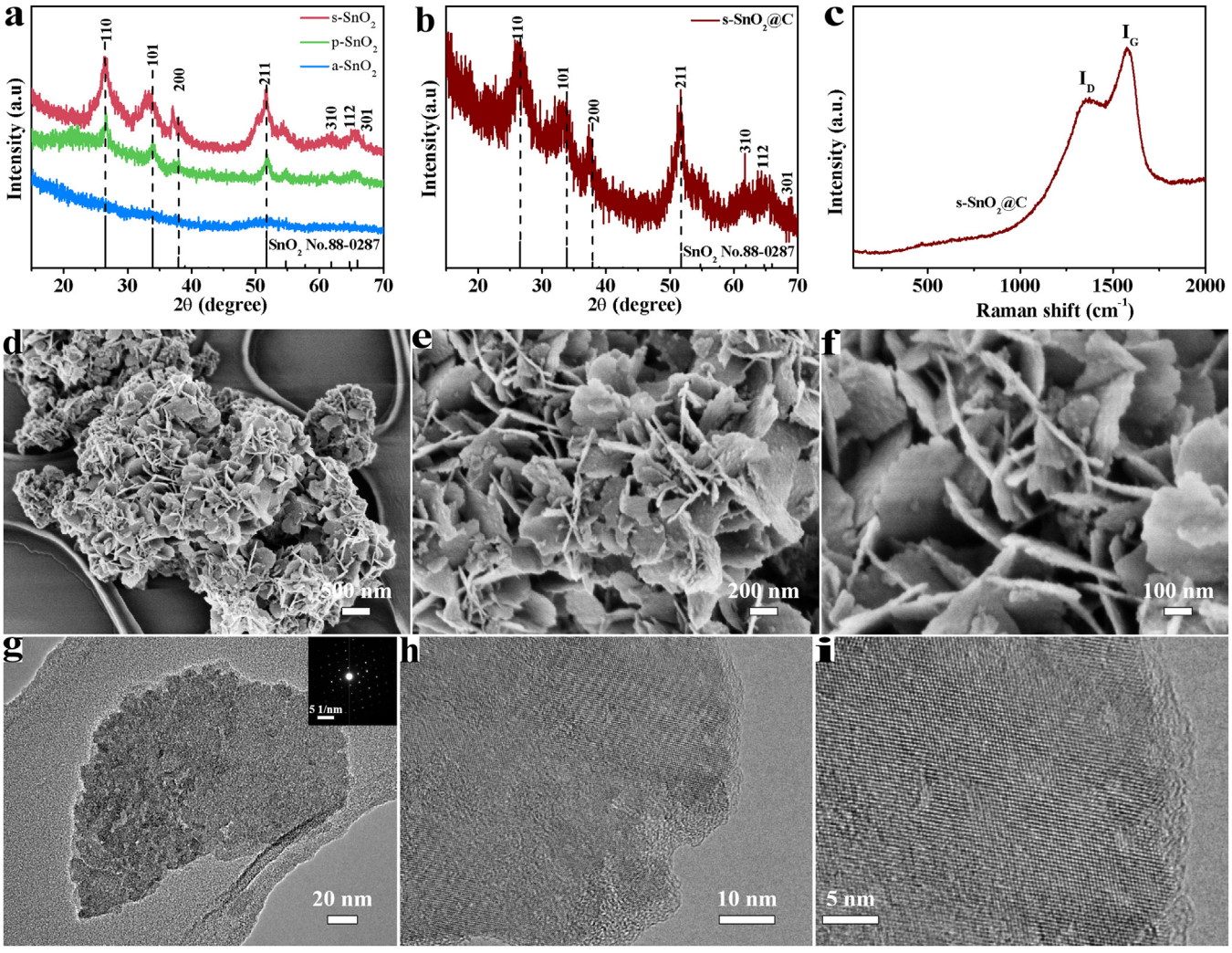

Fig. 3. (a) XRD patterns of s-SnO_2 nanosheets, p-SnO_2 nanosheets, and a-SnO_2 clusters. (b) XRD pattern, (c) Raman spectra, (d–f) SEM, (g) TEM (insets: the corresponding electron-diffraction pattern), and (h, i) HRTEM images of s-SnO_2@C nanosheets.

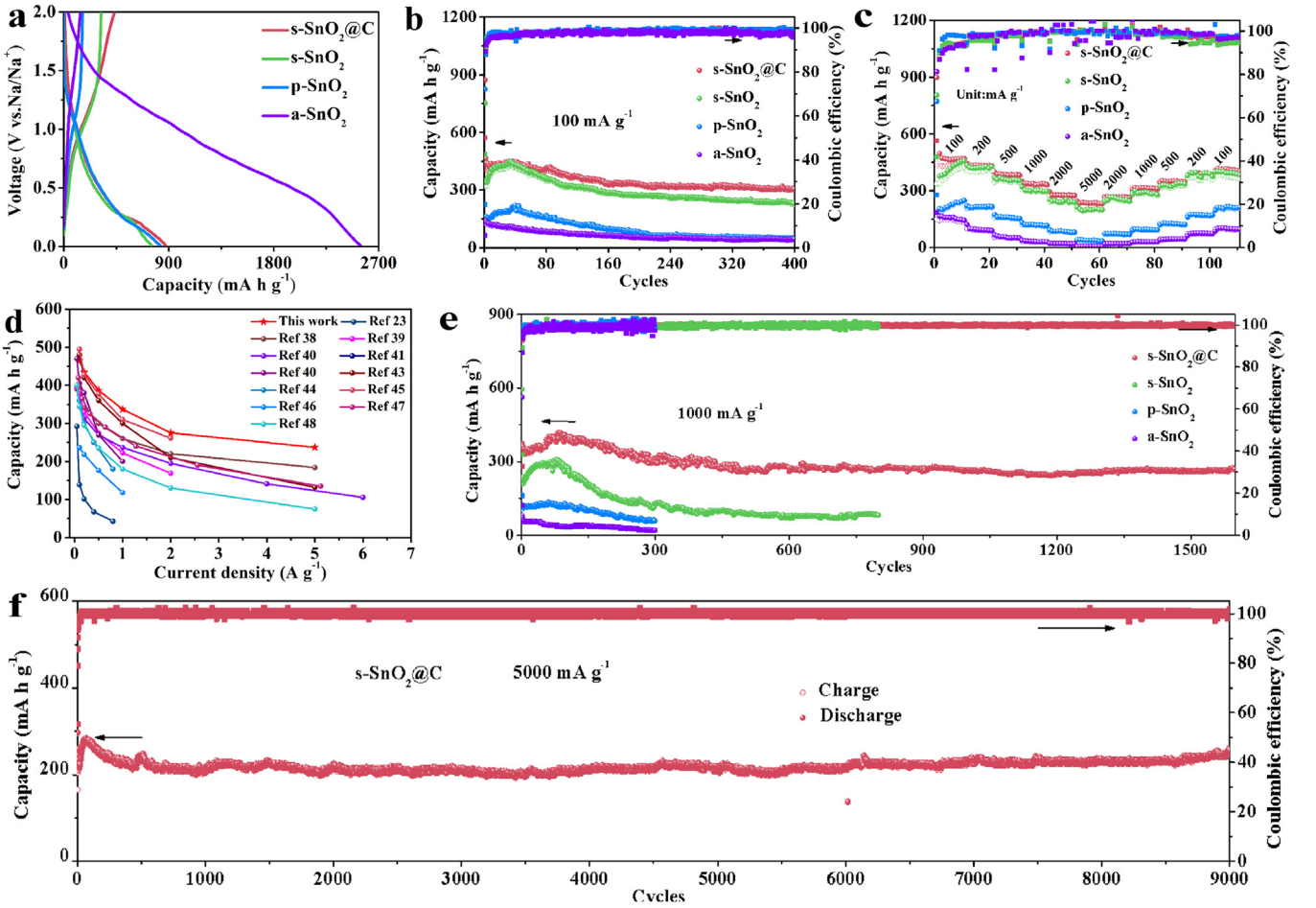

Fig. 4. Electrochemical performances of the as-prepared electrodes in terms of Na^+ storage. (a) The first cycle charge-discharge profiles, (b) cycling performances, and (c) rate capability of s-SnO_2@C nanosheet, s-SnO_2 nanosheet, p-SnO_2 nanosheet, and a-SnO_2 clusters at 100 mA g^{-1}. (d) Capacity versus current density plot of s-SnO_2@C nanosheet with previously reported SnO_2 anode materials for NIBs. (e) Cycling performances of s-SnO_2@C nanosheet, s-SnO_2 nanosheet, p-SnO_2 nanosheet, and a-SnO_2 clusters at 1000 mA g^{-1}. (f) Cycling performances of s-SnO_2@C nanosheet at 5000 mA g^{-1}.

respectively. Furthermore, the s-SnO_2 not only exhibits high initial specific capacity but also presents superior cycling stability compared to p-SnO_2 and a-SnO_2 as shown in Fig. 4(b). As seen clearly, the s-SnO_2 exhibits a slight capacity increase from the 1st cycle to the 35th cycle and a higher specific capacity of 230 mA h g^{-1} in the 400th cycle with a capacity retention of 65.7 % (Fig. S9(b)), while the p-SnO_2 and a-SnO_2 show poor performance with high capacity fade after 400 cycles (Fig. S9(c, d)). The slight capacity increase represented an activation process upon cycling. Finally, the conformally carbon-coated s-SnO_2 nanosheets maintained a higher capacity of 306.2 mA h g^{-1} with a retention of 69.6 % after 400 cycles (Figs. 4(b) and S9(a)), due to the reinforced structural robustness of the uniform carbon layers.

The rate capabilities of single crystalline, polycrystalline, and amorphous structures were further studied to confirm the importance of crystallinity, as shown in Figs. 4(c) and S10. The s-SnO_2 nanosheets display an excellent rate capability. It is capable of delivering substantial capacities of 457.9, 428.3, 368.3, 320, 252.9, and 204.6 mA h g^{-1} at current densities of 100, 200, 500, 1000, 2000, and 5000 mA g^{-1}, respectively. More strikingly, when the current density is reversed back to 100 mA g^{-1} after 100 cycles, a specific discharge capacity of 401.7 mA h g^{-1} is obtained, which is much higher than that of p-SnO_2 nanosheets and a-SnO_2 clusters. For the conformally carbon-coated s-SnO_2 nanosheets, the rate capability was slightly improved compared with s-SnO_2 nanosheets, displaying higher specific capacities of 471.4, 435.7, 387, 337, 275.3, and 235.7 mA h g^{-1} at current densities of 100, 200, 500, 1000, 2000, and 5000 mA g^{-1}, respectively. As shown in the capacity versus current density plot in Fig. 4(d), s-SnO_2@C nanosheets exhibited much higher capacities than most reported SnO_2-based composite materials in NIBs at various current densities [23,40-50]. Fig. 4(e) compares the cycle performances of the four SnO_2-based electrodes at the high current density of 1000 mA g^{-1}. Both the p-SnO_2 and a-SnO_2 electrodes exhibit very low capacities of 59.2 and 20.8 mA h g^{-1} after 300 cycles, respectively. The s-SnO_2 electrode shows a higher capacity of 237.7 mA h g^{-1}, which increased to 308.8 mA h g^{-1} in the first 80 cycles and then decreased to 82.5 mA h g^{-1} after 800 cycles. With the conformal carbon coating on the s-SnO_2 nanosheets, a specific reversible capacity of 268.9 mA h g^{-1} after 1600 cycles was retained with a capacity retention of 72.4 %, demonstrating its superior cycling stability, which was also greatly impacted by the electrolyte [40,41]. Moreover, the s-SnO_2 @C unveiled an ultralong lifespan, maintaining the high capacity of 257.1 mA h g^{-1} and remarkable capacity retention of about 98.9% after 9000 cycles at 5000 mA g^{-1} (Fig. 4(f)), outperforming most reported NIBs anodes (Table S1) based on SnO_2 [23,42-55].

To figure out the reaction and diffusion kinetics of SnO_2 with different crystallinity, cyclic voltammetry (CV) profiles were analyzed using the equation $I = k_1v + k_2v^{1/2}$. This equation separates the capacitive contribution (k_1v) from the diffusion-controlled Faradaic intercalation contribution ($k_2v^{1/2}$), allowing for a more

detailed understanding of the system. Different scan rates were used to obtain these CV profiles. As shown in Figs. 5(a, b) and S11(b–d), all the capacitive contributions of the three samples were no more than 60 % of the total stored charge even at a high scan rate of 6.4 mV s^{-1}, indicating that the electrochemical process is mainly controlled by the intercalation reactions. Therefore, in order to gain a better understanding of the impact of crystallinity on sodium storage performance, we compared the diffusion properties of these SnO_2 materials with varying degrees of crystallinity. As shown in Figs. 5(a) and S11(b, c), it can be observed that increasing the scan rate leads to a gradual shift of the anodic peaks towards higher potential and an increase in peak height. Additionally, the linear correlation between I_p and $v^{1/2}$ suggests that the kinetics of the reaction are governed by the diffusion process of Na^+ ions (Fig. 5(c)) [23]. The Na^+diffusion coefficients of s-SnO_2, p-SnO_2, and a-SnO_2 are estimated as to be 7.16 × 10^{-14}, 1.99 × 10^{-14}, and 1.99 × 10^{-15} cm^2 s^{-1}, respectively. In addition, the chemical diffusion coefficients of Na^+(D_{Na^+}) were assessed through galvanostatic intermittent titration technique (GITT) measurements. Figs. S12, S13, and 5(d) display the GITT curves of s-SnO_2, p-SnO_2, and a-SnO_2 anode during the 1st cycles as a function of capacity in the voltage range of 0.01–2.0 V and the calculated values

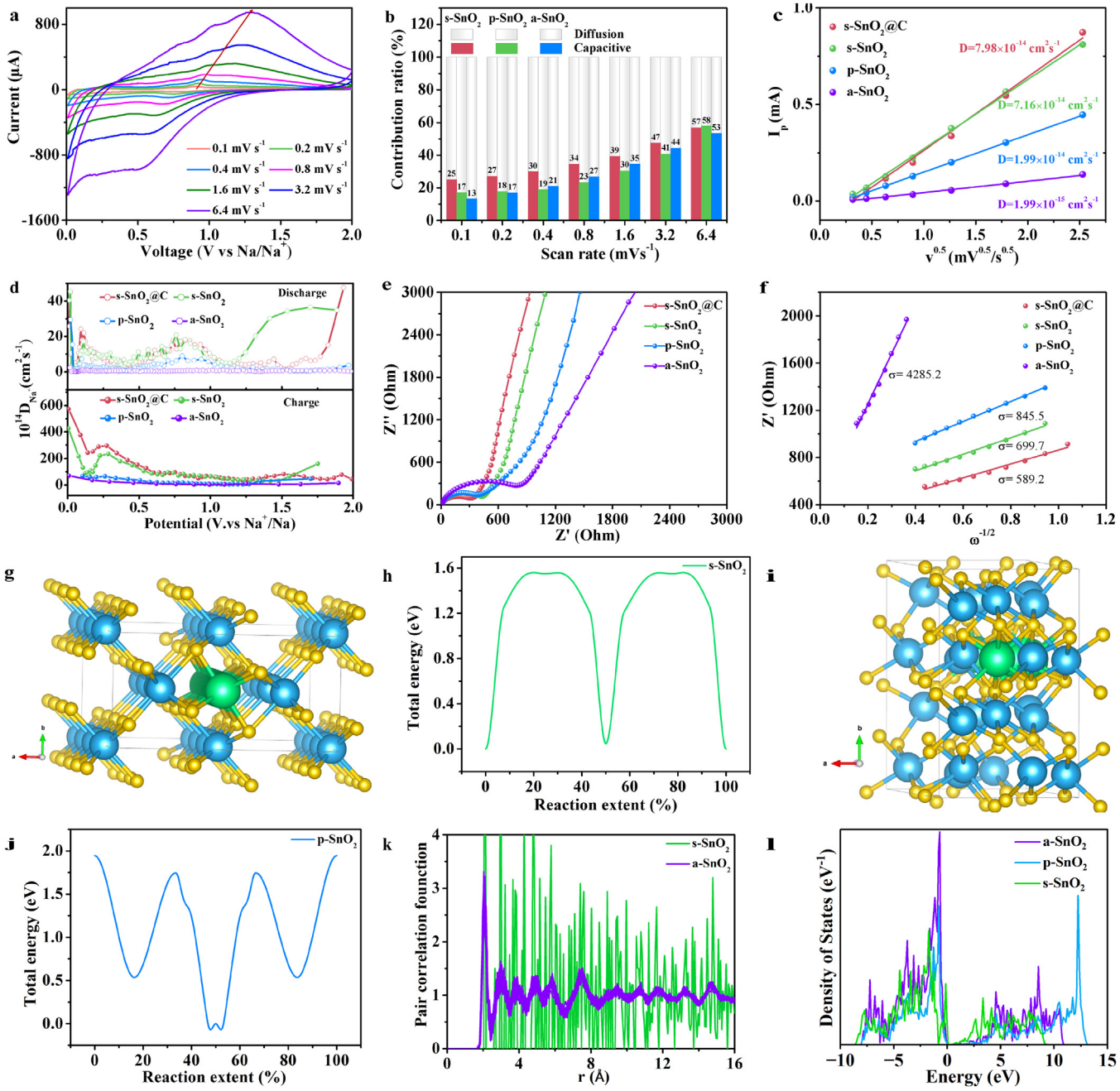

Fig. 5. (a) CV curves of s-SnO_2 nanosheet at different scan rates. (b) Normalized capacitive and diffusion-controlled contribution ratios, (c) Anodic peak current versus square root of the scan rates of s-SnO_2@C, s-SnO_2, p-SnO_2 nanosheet, and a-SnO_2 clusters from 0.1 to 6.4 mV s^{-1}. (d) The chemical diffusion coefficients D_{Na+} versus potential (vs Na^+/Na) plots of s-SnO_2@C, s-SnO_2, p-SnO_2 nanosheet, and a-SnO_2 clusters. (e) EIS of s-SnO_2@C, s-SnO_2, p-SnO_2 nanosheet, and a-SnO_2 clusters anodes. (f) The corresponding plots of the real part of impedance (Z′) as a function of the inverse square root of the angular frequency ($\omega^{-1/2}$) in the Warburg region. Schematic illustration of transport of Na ion in (g) SnO_2 single crystal, (i) SnO_2 polycrystal. (h, j) Energy barriers of Na ion diffusion along the direction [110] computed using the structure models in (g) and in (i), respectively. (k) PDF patterns calculated using the s-SnO_2 and a-SnO_2 models. (l) The calculated densities of states for the s-SnO_2, p-SnO_2 nanosheet, and a-SnO_2 clusters, respectively.

of D_{Na}^+ as a function of potential. As for s-SnO_2, the D_{Na}^+ values lie in the range of 1.57 × 10^{-15} to 4.55 × 10^{-13} cm^{-2} s^{-1} at sodiation state (discharge process) and vary from 3.01 × 10^{-13} to 4.25 × 10^{-12} cm^{-2} s^{-1} at desodiation state (charge process). During most of the potential range, the values of D_{Na}^+ exhibit only a little variation (10^{-14}–10^{-13} cm^{-2} s^{-1}). The p-SnO_2 and a-SnO_2 anodes have smaller values of D_{Na}^+, which are varying from 10^{-15} to 10^{-13} cm^{-2} s^{-1} [44,56]. Both the calculated results of CV and GITT describe that s-SnO_2 performs a faster sodium ion diffusion rate than that of p-SnO_2 and a-SnO_2, demonstrating that the single crystal structure can effectively improve the Na^+ diffusion kinetic. Based on the calculated results of CV and GITT for s-SnO_2@C, the diffusion kinetics is slightly improved with the assistance of the uniform graphitic carbon shell (Figs. 5(c, d) and S11(a)). To gain a more comprehensive understanding of the distinct electrochemical behaviors, we conducted electrochemical impedance spectroscopy (EIS) at a charged state of 2.0 V, as depicted in Fig. 5(e). It is evident that s-SnO_2 exhibits lower impedance values compared to p-SnO_2 and a-SnO_2. As a result of the enhancement in electron conduction and ion transfer at the interface between electrolyte and s-SnO_2 nanosheets, achieved by incorporating a graphitic carbon shell on the surface of s-SnO_2, the impedance values exhibited by s-SnO_2@C are comparatively lower than those observed for s-SnO_2. The EIS curves were fitted by an equivalent circuit and the R_{SEI} values of s-SnO_2@C (302 Ω) and s-SnO_2 (453 Ω) are much lower than that of p-SnO_2 (720 Ω) and a-SnO_2 (997 Ω) (Fig. S14 and Table S2). After activation during the initial five cycles, the R_{SEI} values of s-SnO_2 in the 5th, 10th, 50th, and 100th cycles are 483, 405, 360, and 423 Ω, respectively (Fig. S15 and Table S3), demonstrating its stable surface and solid electrolyte interphase (SEI) film during cycling. The Warburg factor (σ) of s-SnO_2@C and s-SnO_2 anode was calculated to be 589.2 and 699.7, which were smaller than the values of p-SnO_2 (845.5) and a-SnO_2 (4285.2) anodes, highlighting the ultrafast Na^+ diffusion in the s-SnO_2@C and s-SnO_2 material (Fig. 5(f) and Table S2). The fastest Na^+ diffusion of s-SnO_2 nanosheets is ascribed to its continuous Na^+ diffusion channels, while the Na^+ in the p-SnO_2 nanosheets need to transport across abundant grain boundaries, at which the high Na-transfer resistance hinders the diffusion of Na^+(Figs. 5(g, i) and S16) [57].

This was further confirmed by conducting DFT calculations to explore the energy barriers for localized migration and potential diffusion pathways during discharge/charge processes [54]. As depicted in Fig. 5(h, j), the diffusion energy barrier within s-SnO_2 measures only 1.56 eV, significantly lower compared to p-SnO_2 where it reaches 1.95 eV. The a-SnO_2 clusters lack grain boundaries and have fast Na^+diffusion, however, the large number of defects and large agglomerates make the electron transport hindered, which leads to the very low electrochemical activity of a-SnO_2 clusters [27]. As shown in Fig. 5(k, l), there are no states near Fermi energy for a-SnO_2, while the states near Fermi energy for s-SnO_2 are high, demonstrating the low transportation of electrons for a-SnO_2.

In order to deeply understand the sodiation/desodiation mechanism and reversibility of s-SnO_2 electrodes, CV measurements, and ex-situ XRD\in-situ XRD were used to study the SnO_2 electrodes for NIBs. Fig. S17 shows the CV curves of the initial four cycles of s-SnO_2@C, s-SnO_2, p-SnO_2, and a-SnO_2 electrodes. For the s-SnO_2 electrode (Fig. S17(b)), the initial cathodic process exhibits a broad peak within the range of 1.0–1.3 V, which can be attributed to the irreversible formation of solid electrolyte interphase (SEI) film due to electrolyte decomposition on the active material's surface. Additionally, a significant reduction peak between 0.16 and 1.0 V is observed, indicating conversion reactions involving SnO_2→Sn as well as alloying reactions between Na and Sn resulting in Na_xSn formation within the Na_2O matrix [58–60]. During the subsequent anodic process, two distinct peaks at 0.25 and 1.0 V are detected, corresponding to a reversible dealloying reaction of Na_xSn, and oxidation of Sn to SnO_2 [61]. As the discharge-charge process progresses, the cathodic and anodic peaks gradually approach each other and achieve a significantly enhanced reversible electrochemical reaction. Nevertheless, during discharging/charging processes, both p-SnO_2 and a-SnO_2 electrodes exhibit broad peaks, along with substantial irreversible peak areas observed specifically in the initial discharge cycles (Fig. S17(c, d)). For the p-SnO_2 electrode, the anodic peaks shift to higher potentials during the subsequent cycles, resulting in greater polarization and poor reversibility. While the initial cycle of the a-SnO_2 electrode shows reversible conversion and alloying reactions, there is a consistent decrease in the intensity of both cathodic and anodic peaks. This suggests that the sodiation/desodiation processes are not effectively taking place in the a-SnO_2 electrode. Correspondingly, Fig. 6(a, b) summarizes the ex-situ XRD patterns of the s-SnO_2 electrode at various voltages during the first cycle. Clearly, there exist three main characteristic peaks, that is, (110), (101), and (200) at 26.6°, 33.9°, and 37.9°, respectively, for the fresh electrode. As the discharge process advances, the peak intensities corresponding to s-SnO_2 decrease. After the electrode is discharged to 0.01 V, the characteristic peaks of Sn phase are detected. The Na_xSn peaks and another product Na_2O are not observed, which may be due to the amorphous phase lack of associated Bragg peaks. It is worth noting that the peak intensities corresponding to Sn decrease after being charged to 1.5 V, which is replaced by SnO_2 phase. After being charged to 2.0 V, the peaks of Sn disappear, suggesting that the Sn is oxidized and much of the emerging oxide is amorphous [43]. In addition, The in-situ XRD patterns of the s-SnO_2 electrode were collected at different potentials in first cycle and second discharge (Fig. S18). During discharge processes, the peaks of SnO_2 shifted to the left, accompanied by the appearance and enhancement of the Sn peak, indicating that the interplanar spacing of SnO_2 became larger with the insertion of sodium ion and the Sn extrated from the oxide host based on the topotactic reaction. During the charge process, the peaks of SnO_2 were back to the right, accompanied by the weakening and disappearance of the Sn peak, demonstrating that the interplanar spacing of SnO_2 became smaller with the extration of sodium ion and the Sn returned back to the oxide host based on the topotactic reaction.

The evolutions of structures and phases during the conversion reactions were investigated in details using ex-situ HRTEM to understand the electrochemical behaviors and associated reaction kinetics. Metal oxides usually have small particle size and large surface areas. Despite their significant importance, reactions specific to the large surface are generally easily overlooked when investigating metal oxides. A unique conversion reaction is produced on the surface of the s-SnO2 nanosheet and plays a crucial role in the reaction in their bulk material. This reaction initiates at 2.0 V compared to Na^+/Na (Fig. 6(a(0))). A minor capacity (< 5 %) is produced when reaching the activation overpotential (Fig. 6(a(1))). This corresponds to the formation of an unordered layer on the surface consisting of finely divided reaction products (Fig. 6(c, d(1))). This layer can be different from SEI film due its short-range lattice fringes measuring less than 2 nm. The structure of this layer resembles what was previously predicted using molecular dynamics simulations [62]. The mechanism of the unordered layer formation may be that sodium ions insert into the first few atomic layers, leading to lattice disordering and rapid formation of extremely small Sn clusters. The confirmation of anisotropic behavior in various crystallographic orientations has also been observed [62]. A diffuse interface is observed between unordered layer and lattice fringes of single crystal along [110] direction, indicating quick short-range insertion followed by conversion (Fig. 6(c, d(1))). However, this direct conversion process is limited only to the initial few nanometers as it requires uninterrupted supply of

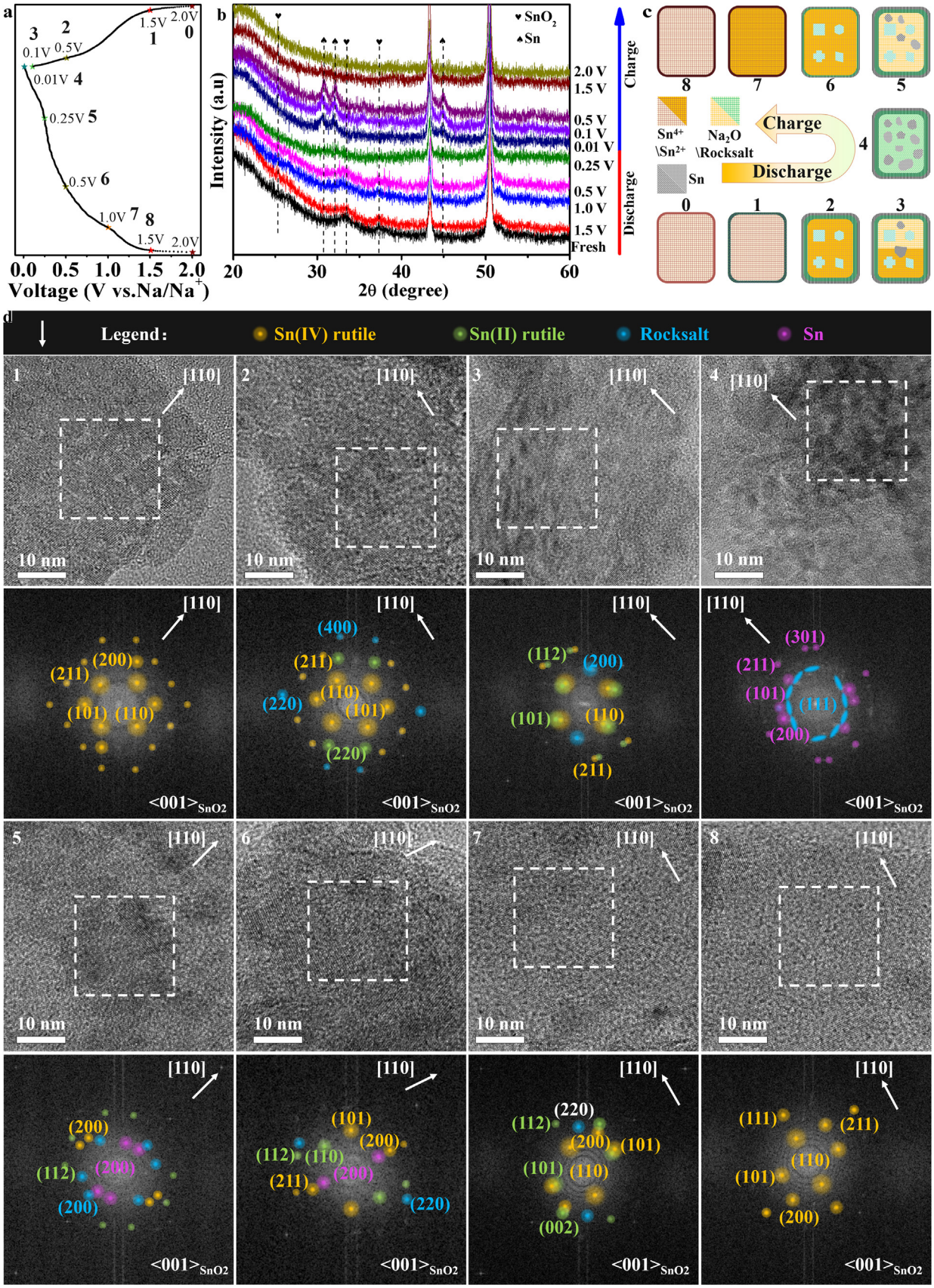

Fig. 6. (a) The galvanostatic profile for the first discharge/charge cycle. (b) Ex-situ XRD. (c) Schematic of the full discharge/charge mechanism representing the ex-situ data points (0–8). (d) Ex-situ HRTEM micrographs and corresponding FFT patterns for samples 1–8. Images for each sample are captured along the $<001>_{SnO2}$ zone axis; the common [110] direction is indicated in the top right of each panel. Diffraction spots are selectively coloured using white pixel intensity according to the legend displayed in the top bar. Dashed white boxes denote the areas over which the FFT has been taken; All FFT patterns are set to the same scale. Scale bars, 20 nm. (0) Discharge 2.0 V, (1) discharge 1.5 V, (2) discharge 0.5 V, (3) discharge 0.25 V, (4) discharge 0.01 V, (5) charge 0.1 V, (6) charge 0.5 V, (7) charge 1.5 V, and (8) charge 2.0 V.

electrons towards reaction front according to our proposed model [62]. However, this assumption becomes invalid once away from the Super-P surface by a small distance. Additionally, sodium diffusion kinetics significantly decrease when the thickness of the converted layer reaches a few nanometres [62]. This can be observed in the rapid decline in cell potential shown in Figs. 6(a(0,1)) and 5(d) [63]. Finally, a distinct reaction mechanism within the bulk becomes necessary due to the limited electron transport occurring beyond the surface. Nonetheless, the development and expansion of this surface layer govern sodium diffusion within the bulk. The kinetics of sodium diffusion also decrease significantly when the thickness of the converted layer reaches a few nanometres (Fig. 6(c, d(2))). At stage 3, an epitaxial double-layered shell forms around the particle core, consisting of a light Na_2O layer encapsulated by a dark metallic Sn layer (Fig. 6(c, d(3))). The interface between Na_2O and SnO_2 is fully coherent, minimizing interfacial free energy through layers arrangement ($Sn|Na_2O|SnO_2$). Inserting Na^+ into crystalline Na_2O or Sn surfaces is not energetically or mechanistically feasible [64]. As this double-layered shell primarily forms on {110} SnO_2 facets, it renders the sides impermeable to sodium early on in the reaction process. Combined with a low energy barrier for diffusion along <001> SnO_2 direction, sodiation proceeds unidirectionally perpendicular to the nanosheet plane (Fig. 6(c, d(4))) [62]. The $Sn|Na_2O$ double-layered shell undergoes minimal changes during discharge. The desodiation process involves the diffusion of sodium out of the nanosheet and the simultaneous insertion of Sn into the Na_2O structure. However, due to its semicoherent interface with Na_2O, sodium inside the shell of the double layer is unable to diffuse outward through Sn, and Sn faces difficulty migrating across this interface (Fig. 6(c, d(5))) [65]. It is only when the battery reaches an almost full charge condition that the shell of the double layer disappears (Fig. 6(c, d(6))). Interestingly, coinciding with its disappearance, the shell converts to a disordered state once again, thereby dispelling the semicoherent $Na_2O|Sn$ interface. Nevertheless, achieving this amorphization requires a significant overpotential and it does not occur until reaching 1.5 V versus Na^+/Na (Fig. 6(c, d(5))) [66].

The $SnO_2 \rightarrow$rutile$\rightarrow$rocksalt$\rightarrow Na_2O$ transformation is a fully topotactic process that involves the insertion and diffusion of cations inside a stable oxide host [37,67–69]. This transformation occurs when charging, with the same orientation relationship observed during the reverse topotactic transformation. However, desodiation necessitates the relocation of the oxide interface to sectors containing Sn and amorphous material. Occasionally, this results in rotated SnO_2 grains due to the formation of new oxide material (Fig. 6(c, d(5–7))). In the full recharge condition, the crystallographic structure and lattice orientation of the initial nanosheet undergoes a near-complete restoration, leading to the re-establishment of a pseudo-single-crystalline nanosheet morphology (Fig. 6(c, d(7))) [39]. This remarkable demonstration of reversibility is further exemplified by the sustained preservation of the nanosheet morphology throughout more than 50 discharge/charge cycles (Fig. S19). The conformal carbon coating on the s-SnO_2 nanosheets can further maintain the single crystalline nanosheet morphology and improve cycle stability.

3. Conclusions

In summary, single-crystal materials have been proposed as an alternative path towards designing advanced conversion anodes, exploring innovative approaches and tactics that go beyond conventional methods aimed at maximizing the efficiency of polycrystalline materials. As an example, SnO_2 with different crystallinities has been successfully synthesized via solvothermal methods and compared to determine the implications of different crystallinity for the electrochemical properties of conversion anodes. The experimental investigations and theoretical studies on SnO_2 with different crystallinities demonstrated that the single-crystal not only shows faster Na^+ diffusion dynamics but also maintains structural stability via topotactic reaction. Further optimization of the electron conduction and structural robustness was realized by uniformly covering a graphitic carbon layer on the surface of s-SnO_2 nanosheets. Thorough investigations utilizing operando techniques such as ex-situ XRD and TEM have been conducted to gain a deep understanding of the topotactic reaction in a single crystal conversion anode. The aim is to pave the way for the advancement of electrode materials that exhibit exceptional cycling stability and rate performance.

4. Experimental section

4.1. Synthesis of s-SnO_2 nanosheets and s-SnO_2@C nanosheets

In a typical procedure, 5 mmol of $SnCl_2{\cdot}2H_2O$ was initially introduced into 40 mL of ethanolamine. After vigorous agitation for 30 min, the $SnCl_2{\cdot}2H_2O$ dissolved in ethanolamine to form a transparent solution, which was then transferred into a Teflon-lined autoclave with a capacity of 50 mL. The autoclave was sealed and heated at a temperature of 180 °C for a duration of 48 h. Subsequently, the system was allowed to naturally cool down to room temperature before collecting the final product through centrifugation. The collected mixture underwent multiple washes using distilled water and absolute ethanol, followed by overnight vacuum drying for further characterization.

To obtain s-SnO_2@C nanosheets, we first dispersed 1.0 g of prepared s-SnO_2 powders in an aqueous solution containing tris(hydroxymethyl)aminomethane (Tris) with pH value set at 8.5 through stirring. Next, we dissolved 160 mg of dopamine in deionized water (10 mL). This dopamine solution was gradually added dropwise into the aqueous dispersion containing s-SnO_2 nanosheets while continuously stirring the mixture for polymerization over a period of 24 h. Following this step, polydopanine-coated s-SnO_2 (s-SnO_2@PDA) powders were subjected to three rounds of washing using deionized water and separated via centrifugation before being dried under vacuum conditions at a temperature of 90 °C for approximately 12 h. The collected s-SnO_2@PDA powders were subsequently calcined under argon atmosphere in a tube furnace at temperatures reaching up to 450 °C over a span of two hours. Following calcination, the formation of s-SnO@C was achieved.

4.2. Synthesis of p-SnO_2 nanosheets

In a typical procedure, 5 mmol of $SnCl_2{\cdot}2H_2O$ was initially introduced into 40 mL of ethanolamine. After vigorous agitation for 30 min, the $SnCl_2{\cdot}2H_2O$ was completely dissolved in ethanolamine to yield a transparent solution. This solution was then transferred into a Teflon-lined autoclave with a capacity of 50 mL, sealed tightly, and subjected to stirring and heating at a temperature of 180 °C for a duration of 48 h. Subsequently, the system was allowed to naturally cool down to room temperature before collecting the final product through centrifugation. The resulting mixture underwent multiple washes using distilled water and absolute ethanol, followed by overnight vacuum drying for further characterization.

4.3. Synthesis of a-SnO_2 clusters

In a typical procedure, $SnCl_2{\cdot}2H_2O$ (Alfa Aesar, 98 %) was introduced into a basic mixture comprising ethanol and water ($V_{ethanol}$:V_{water} = 1:1) to achieve a concentration of Sn(II) at

15.8 mM. The resulting suspension appeared as a white turbid solution and was subjected to magnetic stirring for one hour before being transferred to an autoclave made of stainless steel with Teflon lining. Subsequently, the mixture was heated at 120 °C for a duration of 30 min. Following centrifugation, a light yellow product was obtained and subsequently dried overnight at room temperature (25 °C).

4.4. Materials characterizations

The X-ray diffraction analysis of the powdery composite was conducted using a D8 Advance instrument from Bruker AXS, employing Cu Kα radiation. Additionally, the phase structures were examined using a Jobin Yvon Horiba Raman spectrometer model HR800 equipped with a 10-mW helium/neon laser operating at an excitation wavelength of 632.8 nm within the spectral range of 100 to 2000 cm^{-1}. The XPS peaks were analyzed by fitting them with a background similar to the "Shirley" model and Gaussian-Lorentzian peaks. The morphology of the samples was determined using an FE-SEM instrument (JEOL 7500FA, Tokyo, Japan). To investigate the microstructure and perform elemental mapping, Energy-filtered TEM (JEOL 2011 F, Tokyo, Japan) was employed. Ex-situ samples representing different discharge and charge states were prepared at a current density of 100 mA g^{-1}. After allowing the coin cells to rest post-cycling, they were opened in a glovebox filled with argon. The electrodes in use were taken out, dried off, and kept in dimethyl carbonate for XRD analysis. The electrodes for XRD analysis were then placed into anhydrous NMP to redistribute the electrode material for TEM measurements.

4.5. Electrochemical characterization

The electrochemical tests were conducted using 2032 coin-type half cells, where sodium metal was utilized as the counter electrode within an Argon-filled glove box. To prepare the composites, slurries containing s-SnO2 and s-SnO2@C active materials (70 wt%), Super P acetylene black (20 wt%), and carboxymethyl cellulose (CMC, 10 wt%) were coated onto copper foil. The electrodes had a mass loading of approximately 1.0–1.5 mg cm^{-2}. Electrodes were produced using p-SnO_2 and a-SnO_2 as the active materials, following the same procedure. For comparison purposes, we utilized an electrolyte composed of 1 mol L^{-1} $NaClO_4$ in a mixture of ethylene carbonate and diethyl carbonate (in a 1:1 vol ratio), along with fluoroethylene carbonate (FEC) at a concentration of 5 wt%. Galvanostatic charge/discharge and GITT tests were conducted on a Land battery tester within the voltage range of 0.01 to 2.0 V versus Na/Na^+. The current densities employed were determined based on the overall mass of composites. The electrochemical workstation CHI 660D was utilized to conduct cyclic voltammetry (CV) in the voltage range of 0.01–2.0 V. Additionally, AC electrochemical impedance spectroscopy (EIS) measurements were performed using the same CHI 660D instrument. The AC signal amplitude applied for EIS analysis was set at 5 mV, while the frequency range varied from 100 kHz to 0.01 Hz during measurement.

4.6. Computational method

DFT calculations were performed using the Vienna ab initio simulation package (VASP) with the projector-augmented wave (PAW) method [70–73] The Perdew-Burke-Ernzerhof (PBE) functional, which incorporates the generalized gradient approximation (GGA), was utilized to describe the exchange-correlation interaction [74]. To account for dispersion interactions, we employed the DFT-D3 van der Waals correction proposed by Grimme [75]. A plane wave energy cut-off of 550 eV was applied, and a Gamma-centered k-points mesh with a Kmesh-Resolved value of 0.03 2π $Å^{-1}$ was used for all calculations. Convergence criteria were set at forces and total energy on all atoms below 0.05 eV $Å^{-1}$ and 1×10^{-5} eV, respectively. Spin-polarization was considered in all calculations as well. A pristine structure consisting of 16 Sn atoms and 32 O atoms was constructed using a $2 \times 1 \times 4$ supercell. To create a polycrystalline structure, the *b*-axis of the supercell was rotated by $\pm$ 33.8675° at its midpoint. The Climbing Image Nudged Elastic Band (CINEB) method was employed to simulate the kinetic process, with six intermediate structures inserted between the initial and final states as transition states [76,77].

Declaration of competing interest

The authors declare the following financial interests/personal relationships which may be considered as potential competing interests: Xuebin Yu reports financial support was provided by National Natural Science Foundation of China. Xuebin Yu reports financial support was provided by Innovation Program of Shanghai Municipal Education Commission.

CRediT authorship contribution statement

Weili Liu: Writing – review & editing, Writing – original draft, Conceptualization. **Tian Xu:** Software, Formal analysis, Data curation. **Shouguo Wang:** Supervision. **Guanglin Xia:** Supervision. **Dalin Sun:** Supervision, Data curation. **Xuebin Yu:** Supervision, Funding acquisition, Conceptualization.

Acknowledgements

This work was partially supported by the National Natural Science Foundation of China (No. 51971065) and the Innovation Program of Shanghai Municipal Education Commission (No. 2019-01-07-00-07-E00028). The authors would like to thank SCI-GO (www.sci-go.com) for the XPS analysis.

Supplementary materials

Supplementary material associated with this article can be found, in the online version, at doi:10.1016/j.jmst.2024.09.013.

References

[1] C.L. Li, K.Y. Chen, X.J. Zhou, J. Maier, npj Comput. Mater. 4 (2018) 22–37.
[2] S.-H. Yu, X.R. Feng, N. Zhang, J. Seok, H.D. Abruña, Acc. Chem. Res. 51 (2018) 273–281.
[3] F. Wang, S.-W. Kim, D.-H. Seo, K. Kang, L.P. Wang, D. Su, J.J. Vajo, J. Wang, J. Graetz, Nat. Commun. 6 (2015) 6668–6677.
[4] F. Badway, F. Cosandey, N. Pereira, G.G. Amatucci, J. Electrochem. Soc. 150 (2003) A1318–A1327.
[5] P. Poizot, S. Laruelle, S. Grugeon, L. Dupont, J.-M. Tarascon, Nature 407 (2000) 496–499.
[6] J. Cabana, L. Monconduit, D. Larcher, M.Rosa Palacín, Adv. Mater. 22 (2010) E170–E192.
[7] M. Stanley Whittingham, Chem. Rev. 114 (2014) 11414–11443.
[8] F. Wang, R. Robert, N.A. Chernova, N. Pereira, F. Omenya, F. Badway, X. Hua, M. Ruotolo, R.G. Zhang, L.J. Wu, V. Volkov, D. Su, B. Key, M.S. Whittingham, C.P. Grey, G.G. Amatucci, Y.M. Zhu, J. Graetz, J. Am. Chem. Soc. 133 (2011) 18828–18836.
[9] F. Wang, H.-C. Yu, M.-H. Chen, L.J. Wu, N. Pereira, K. Thornton, A.V. Ven, Y.M. Zhu, G.G. Amatucci, J. Graetz, Nat. Commun. 3 (2012) 1201–1209.
[10] W. Zhang, D.C. Bock, C.J. Pelliccione, Y. Li, L.J. Wu, Y.M. Zhu, A.C. Marschilok, E.S. Takeuchi, K.J. Takeuchi, F. Wang, Adv. Energy Mater. 6 (2016) 1502471.
[11] H.-C. Yu, F. Wang, G.G. Amatucci, K. Thornton, J. Phase Equilib. Diffus. 37 (2016) 86–99.
[12] L.S. Li, R. Jacobs, P. Gao, L.Y. Gan, F. Wang, D. Morgan, S. Jin, J. Am. Chem. Soc. 138 (2016) 2838–2848.
[13] R.E. Doe, K.A. Persson, Y.S. Meng, G. Ceder, Chem. Mater. 20 (2008) 5274–5283.
[14] J.K. Ko, K.M. Wiaderek, N. Pereira, T.L. Kinnibrugh, J.R. Kim, P.J. Chupas, K.W. Chapman, G.G. Amatucci, ACS Appl. Mater. Interfaces 6 (2014) 10858–10869.
[15] D.H. Chang, M.-H. Chen, A.V. Ven, Chem. Mater. 27 (2015) 7593–7600.
[16] S. Kim, J.Y. Liu, K. Sun, J.J. Wang, S.J. Dillon, P.V. Braun, Adv. Funct. Mater. 27 (2017) 1702783.

[17] M. Gu, A. Kushima, Y.Y. Shao, J.-G. Zhang, J. Liu, N.D. Browning, J. Li, C.M. Wang, Nano Lett. 13 (2013) 5203–5211.
[18] J.Y. Huang, L. Zhong, C.M. Wang, J.P. Sullivan, W. Xu, L.Q. Zhang, S.X. Mao, N.S. Hudak, X.H. Liu, A. Subramanian, H. Fan, L. Qi, A. Kushima, J. Li, Science 330 (2010) 1515.
[19] S. Chen, M. Wang, J. Ye, J. Cai, Y. Ma, H. Zhou, L. Qi, Nano Res. 6 (2013) 243–252.
[20] L. Zhang, G. Zhang, H.B. Wu, L. Yu, X.W. Lou, Adv. Mater. 25 (2013) 2589–2593.
[21] C. Wang, Y. Zhou, M.Y. Ge, X.B. Xu, Z.L. Zhang, J.Z. Jiang, J. Am. Chem. Soc. 132 (2010) 46–47.
[22] Z.T. Li, J.Z. Feng, H. Hu, Y.F. Dong, H. Ren, W.T. Wu, Z.P. Hu, M.B. Wu, J. Mater. Chem. A 6 (2018) 18920–18927.
[23] L.L. Fan, X.F. Li, B. Yan, J.M. Feng, D.B. Xiong, D.J. Li, L. Gu, Y.R. Wen, S. Lawes, X.L. Sun, Adv. Energy Mater. 6 (2016) 1502057.
[24] J. Lee, J.K. Papp, R.J. Clément, S. Sallis, Dd-H. Kwon, T. Shi, W.L. Yang, B.D. McCloskey, G. Ceder, Nat. Commun. 8 (2017) 981.
[25] X. Yang, R.-Y. Zhang, J. Zhao, Z.-X. Wei, Dd-X. Wang, X.-F. Bie, Y. Gao, J. Wang, F. Du, G. Chen, Adv. Energy Mater. 8 (2018) 1701827.
[26] Y. Choi, C. Jo, W.-G. Lim, J.-C. Han, B.-G. Chae, C.G. Park, J. Lee, J.K. Kim, ACS Nano 13 (2019) 6513–6521.
[27] J.E. Medvedeva, D.B. Buchholz, R.P.H. Chang, Adv. Electron. Mater. 3 (2017) 1700082.
[28] Y. Huang, Z. Lin, M. Zheng, T. Wang, J. Yang, F. Yuan, X. Lu, L. Liu, D. Sun, J. Power Sources 307 (2016) 649–656.
[29] W. Cheng, F. Rechberger, G. Ilari, H. Ma, W.-I. Lin, M. Niederberger, Chem. Sci. 6 (2015) 6908–6915.
[30] X.M. Fan, G.R. Hu, B. Zhang, X. Ou, J.F. Zhang, W.G. Zhao, H.P. Jia, L.F. Zou, P. Li, Y. Yang, Nano Energy 70 (2020) 104450.
[31] G.N. Qian, Y.T. Zhang, L.S. Li, R.X. Zhang, J.M. Xu, Z.J. Cheng, S.J. Xie, H. Wang, Q.L. Rao, Y.S. He, Y.B. Shen, L.W. Chen, M. Tang, Z.-F. Ma, Energy Storage Mater. 27 (2020) 140–149.
[32] J. Li, H.Y. Li, W. Stone, R. Weber, S. Hy, J.R. Dahn, J. Electrochem. Soc. 164 (2017) A3529–A3537.
[33] J. Li, A.R. Cameron, H.Y. Li, S. Glazier, D.J. Xiong, M. Chatzidakis, J. Allen, G.A. Botton, J.R. Dahn, J. Electrochem. Soc. 164 (2017) A1534–A1544.
[34] Y.J. Bi, J.H. Tao, Y.Q. Wu, L.Z. Li, Y.B. Xu, E.Y. Hu, B.B. Wu, J.T. Hu, C.M. Wang, J.-G. Zhang, Y. Qi, J. Xiao, Science 370 (2020) 1313–1317.
[35] B.Z. You, Z.X. Wang, F. Shen, Y.J. Chang, W.J. Peng, X.H. Li, H.J. Guo, Q.Y. Hu, C.W. Deng, S. Yang, G.C. Yan, J.X. Wang, Small 5 (2021) 2100234.
[36] Z.H. Song, H. Li, W. Liu, H.Z. Zhang, J.W. Yan, Y.F. Tang, J.Y. Huang, H.M. Zhang, X.F. Li, Adv. Mater. 32 (2020) 2001001.
[37] B. Cheng, J.M. Russell, W.S. Shi, L. Zhang, E.T. Samulski, J. Am. Chem. Soc. 126 (2004) 5972–5978.
[38] Y.F. Sun, F.C. Lei, S. Gao, B.C. Pan, J.F. Zhou, Y. Xie, Angew. Chem. Int. Ed. 52 (2013) 10569–10572.
[39] A.W. Xiao, H.J. Lee, I. Capone, A. Robertson, T.-U. Wi, J. Fawdon, S. Wheeler, H.-W. Lee, N. Grobert, M. Pasta, Nat. Mater. 19 (2020) 644–654.
[40] Y.Y. Hu, H.W. Fu, Y.H. Geng, X.T. Yang, L. Fan, J. Zhou, B.A. Lu, Angew. Chem. Int. Ed. 63 (2024) e202403269.
[41] X.M. Ma, H.W. Fu, J.Y. Shen, D.W. Zhang, J.W. Zhou, C.Y. Tong, A.M. Rao, J. Zhou, L. Fan, B.A. Lu, Angew. Chem. Int. Ed. 135 (2023) e202312973.
[42] J. Niu, J.J. Liang, A. Gao, M.L. Dou, Z.P. Zhang, X. Lu, F. Wang, J. Mater. Chem. A 7 (2019) 21711–21721.
[43] H.-G. Wang, Q. Wu, Y.H. Wang, X. Wang, L.L. Wu, S.Y. Song, H.J. Zhang, Adv. Energy Mater. 9 (2019) 1802993.
[44] Y. Cheng, S.H. Wang, L. Zhou, L.M. Chang, W.Q. Liu, D.M. Yin, Z. Yi, L.M. Wang, Small 16 (2020) 2000681.
[45] Y.-X. Wang, Y.-G. Lim, M.-S. Park, S.-L. Chou, J.H. Kim, H.-K. Liu, S.-X. Dou, Y.-J. Kim, J. Mater. Chem. A 2 (2014) 529–534.
[46] J. Cui, Z.-L. Xu, S.S. Yao, J.Q. Huang, J.-Q. Huang, S. Abouali, M. Akbari Garakani, X.H. Ning, J.-K. Kim, J. Mater. Chem. A 4 (2016) 10964–10973.
[47] J. Patra, H.-C. Chen, C.-H. Yang, C.-T. Hsieh, C.-Y. Su, J.-K. Chang, Nano Energy 28 (2016) 124–134.
[48] R.S. Kalubarme, J.-Y. Lee, C.-J. Park, ACS Appl. Mater. Interfaces 7 (2015) 17226–17237.
[49] M. Dirican, Y. Lu, Y.Q. Ge, O. Yildiz, X.W. Zhang, ACS Appl. Mater. Interfaces 7 (2015) 18387–18396.
[50] A. Jahel, C.M. Ghimbeu, A. Darwiche, L. Vidal, S.H. Garreau, C. Vix-Guterlac, L. Monconduit, J. Mater. Chem. A 3 (2015) 11960–11969.
[51] Y. Yang, Z.-Z. Pan, Y.-Y. Wang, Y.-C. Ma, C. Li, Y.-J. Lua, X.-L. Wu, Nanoscale 11 (2019) 14616–14624.
[52] X.X. Chen, R.Z. Cai, P.G. Liu, W.F. Liu, K.Y. Liu, ChemistrySelect 6 (2021) 3192–3198.
[53] X. Zhao, M. Luo, W.X. Zhao, R.M. Xu, Y. Liu, H. Shen, ACS Appl. Mater. Interfaces 10 (2018) 38006–38014.
[54] J. Ding, Z. Li, H.L. Wang, K. Cui, A. Kohandehghan, X.H. Tan, D. Karpuzovc, D. Mitlin, J. Mater. Chem. A 3 (2015) 7100–7111.
[55] Y.-N. Sun, M. Goktas, L. Zhao, P. Adelhelm, B.-H. Han, J. Colloid Interface Sci. 572 (2020) 122–132.
[56] G. Ali, S.A. Patil, S. Mehboob, M. Ahmad, H.Y. Ha, H.-S. Kim, K.Y. Chung, J. Power Sources 419 (2019) 229–236.
[57] Y. Nomura, K. Yamamoto, T. Hirayama, E. Igaki, K. Saitoh, ACS Energy Lett. 5 (2020) 2098–2105.
[58] D.Y.W. Yu, P.V. Prikhodchenko, C.W. Mason, S.K. Batabyal, J. Gun, S. Sladkevich, A.G. Medvedev, O. Lev, Nat. Commun. 4 (2013) 2922.
[59] J.F. Mao, X.L. Fan, C. Luo, C.S. Wang, ACS Appl. Mater. Interfaces 8 (2016) 7147–7155.
[60] Y.C. Lu, C. Ma, J. Alvarado, T. Kidera, N. Dimov, Y.S. Meng, S. Okada, J. Power Sources 284 (2015) 287–295.
[61] D.T. Ma, Y.L. Li, H.W. Mi, S. Luo, P.X. Zhang, Z.Q. Lin, J.Q. Li, H. Zhang, Angew. Chem. Int. Ed. 57 (2018) 8901–8905.
[62] Y. Ma, S.H. Garofalini, J. Am. Chem. Soc. 134 (2012) 8205–8211.
[63] J. Newman, K.E. Thomas-Alyea, Electrochemical Systems, 3rd ed., Wiley, Hoboken, New Jersey, 2004.
[64] Y. Ma, S.H. Garofalini, Phys. Chem. Chem. Phys. 16 (2014) 11690–11697.
[65] D.A. Porter, K.E. Easterling, M.Y. Sherif, Phase Transformations in Metals and Alloys, 3rd ed., Taylor & Francis, Oxford, UK, 2009.
[66] W.M. Haynes, D.R. Lide, T.J. Bruno, CRC Handbook of Chemistry and Physics, CRC Press, Oxford, UK, 2016.
[67] K. Karki, L.J. Wu, Y. Ma, M.J. Armstrong, J.D. Holmes, S.H. Garofalini, Y.M. Zhu, E.A. Stach, F. Wang, J. Am. Chem. Soc. 140 (2018) 17915–17922.
[68] W. Zhang, Y. Li, L.J. Wu, Y.D. Duan, K. Kisslinger, C.L. Chen, D.C. Bock, F. Pan, Y.M. Zhu, A.y C. Marschilok, E.S. Takeuchi, K.J. Takeuchi, F. Wang, Nat. Commun. 10 (2019) 1972.
[69] X. Hua, P.K.A.C. Gong, P.A. Chater, E.M. Schmidt, H.S. Geddes, A.W. Robertson, P.G. Bruce, A.L. Goodwin, Nat. Commun. 12 (2021) 561.
[70] P.E. Blochl, Phys. Rev. B 50 (1994) 17953–17979.
[71] G. Kresse, J. Hafner, Phys. Rev. B 49 (1994) 14251–14269.
[72] G. Kresse, J. Furthmüller, Comp. Mater. Sci. 6 (1996) 15–50.
[73] G. Kresse, D. Joubert, Phy. Rev. B 59 (1999) 1758.
[74] P.P. John, B. Kieron, E. Matthias, Phy. Rev. Lett. 77 (1996) 3865–3868.
[75] S. Grimme, J. Antony, S. Ehrlich, H. Krieg, J. Chem. Phys. 132 (2010) 154104.
[76] A. Heyden, A.T. Bell, F.J. Keil, J. Chem. Phys. 123 (2005) 224101.
[77] J. Paier, R. Hirschl, M. Marsman, G. Kresse, J. Chem. Phys. 122 (2005) 234102.